Arabian Journal of Chemistry (2022) **15**, 103566

King Saud University

Arabian Journal of Chemistry

www.ksu.edu.sa
www.sciencedirect.com

ORIGINAL ARTICLE

Two new luminescent coordination polymers: Therapeutic effects on angina pectoris

Jing Li [a,b,1], Jing-Wei Yuan [c,1], Hai-Bo Yu [c], Yu-Ming Kang [a,*], Qing-Ling Su [d]

[a] *Department of Physiology and Pathophysiology, Xi'an Jiaotong University School of Basic Medical Sciences, Key Laboratory of Environment and Genes Related to Diseases of Education Ministry of China, Xi'an 710061, China*
[b] *Department of Physiology, Jiamusi University Basic Medical College, Jiamusi 154002, China*
[c] *Department of Cardiovascular Medicine, First Affiliated Hospital of Jiamusi University, Jiamusi 154002, China*
[d] *Department of Medicine, People's Hospital, Taiyuan 030012, China*

Received 26 June 2021; accepted 9 November 2021
Available online 12 November 2021

KEYWORDS

Hydrothermal sysnthesis;
Luminescence;
Angina pectoris;
Endothelial cells

Abstract By tuning the central metal ions from Zn(II) to Cd(II), two new coordination polymers was acquired in success, namely $\{(H_3O)[Zn_4(bptc)_3(3\text{-bpmh})]\}_n \cdot 6n(H_2O)$ (**1**) and $[Cd_3(bptc)(3\text{-bpmh})(H_2O)_4] \cdot 4(H_2O)$ (**2**) (H_3bptc = biphenyl-3,4′,5-tricarboxylic acid, 3-bpmh = N,N-bis-pyridin-3-ylmethylene-hydrazine), under hydrothermal conditions. The luminescent properties investigations showed that **1**–**2** emit intense luminescence with different maximum emission peaks. Their therapeutic and nursing protective effects on angina pectoris were assessed and we also discussed the corresponding mechanism simultaneously. The content of Interleukin-6 (IL-6) and soluble vascular cell adhesive molecule (SVCAM-1) released by endothelial cells (EC) was discovered through enzyme linked immunosorbent assay (ELISA) detection kit. Besides, the activation of Notch signaling pathway was also evaluated by the real time reverse transcription-polymerase chain reaction (RT-PCR). Influence of compounds on the peripheral blood white blood cell (WBC) numbers was measured with flow cytometry. We utilized optical coherence tomography (OCT) to measure the thickness of the fibrous cap of atherosclerotic plaque in patients with angina pectoris.

1. Introduction

Coronary heart disease has become a common and frequently-occurring disease, with the characteristics of high morbidity and mortality (Fuchs and Becker, 1982). Endothelial cells (EC) in blood vessels have a significant importance on coronary heart disease development. Occurrence and development of angina pectoris involve inflammation and blood coagulation. Certain cell adhesion molecules, cytokines and coagulation factors play a certain role in the occurrence and course of angina pectoris, such as SVCAM-1 and IL-6 (Kelemen, 2006; Zuchi et al., 2013).

* Corresponding author.
E-mail address: yumingkang66@163.com (Y.-M. Kang).
[1] Authors are contributed equally to this work.
Peer review under responsibility of King Saud University.

Production and hosting by Elsevier

https://doi.org/10.1016/j.arabjc.2021.103566
1878-5352 © 2021 The Authors. Published by Elsevier B.V. on behalf of King Saud University.

MOFs composed of organic backbones together with metal ions have drawn attention of modern scholars not only because of their fascinating topological architectures but also because of their potential utilization regarding of heterogeneous catalysis, magnetism, luminescence sensing, gas storage, etc (Fan et al., 2021; Fan et al., 2022; Wang et al., 2021; Zhao et al., 2021; Zhang et al., 2020; Li et al., 2020). According to the reports, it can be found that the structures of MOFs are highly sensitive to geometric configurations of metal ions, organic ligands with various bridging modes and spatial conformations, as well as various reaction conditions (Li et al., 2020; Luo et al., 2010; Qin et al., 2008; Ma et al., 2021; Ran et al., 2021; Ma et al., 2019). Thus, the challenge regarding of framework of MOFs with expected structures together with desired properties still exists to chemists. To gain the goal of controllable synthesis at molecular level, it is requirement for us to careful selection of suitable organic ligands with multi-coordination sites and metal ions with defined coordination polyhedrons (Guo et al., 2019; Wang et al., 2021; Fan et al., 2022; Zhang et al., 2013; Yang et al., 2016). During the past few decades, the combination of polycarboxylate and electrically neutral N-donor auxiliary ligands is extensively applied in structure of MOFs with high thermal stabilities and promising properties, and the structures and properties of MOFs are able to be adjusted in ease by changing the polycarboxylate ligands or N-donor auxiliary ligands (Zhang et al., 2020; Feng et al., 2017; Feng et al., 2015; Bu et al., 2014; Yang et al., 2013). The structural complementary two ligands may synergistically connected metal ions into desired extended frameworks that have better performance compared to the solitary ligand-based MOFs (Zhang et al., 2008).

Bearing the above-mentioned thoughts in mind, C_2-symmetric tricarboxylate ligand (biphenyl-3,4′,5-tricarboxylic acid) and a long dipyridyl ligand (N,N-bis-pyridin-3-ylmethylene-hydrazine) were selected as the organic building backbones to construct new MOFs in this study. *Via* tuning the metal ions from Zn(II) to Cd(II), two coordination polymers were acquired in success, namely $\{(H_3O)[Zn_4(bptc)_3(3\text{-bpmh})]\}_n\cdot 6n(H_2O)$ (**1**) and $[Cd_3(bptc)(3\text{-bpmh})(H_2O)_3]_n\cdot 4n(H_2O)$ (**2**) (H_3bptc = biphenyl-3,4′,5-tricarboxylic acid, 3-bpmh = N,N-bis-pyridin-3-ylmethylene-hydrazine), under hydrothermal conditions. Their luminescent properties, crystal structures, thermal, together with syntheses were demonstrated in the following. We conducted biological experiments in this research to determine therapeutic and nursing protective effects of the compounds on angina.

2. Experimental

2.1. Materials and instrumentation

Overall chemical agents employed in our investigation are of analytical class and commercially available. Through the utilization of an elemental Vario EL III analyzer, Elemental analyses including C, H along with N were completed. The powder diffractometer of PANalytical X'Pert Pro was applied for the analysis of PXRD with 0.05° step size using the Cu/Kαradiation (with λ of 1.54056 Å). The TGA for **1**–**2** were finished through employing the NETSCHZ STA-449C under nitrogen atmosphere heating rate in 30 to 800 °C temperature. The luminescent experiments for **1**–**2** and organic ligand were implemented with Edinburgh FLS920 TCSPC fluorescence spectrophotometer in the environment of room temperature.

2.2. Synthesis of $\{(H_3O)[Zn_4(bptc)_3(3\text{-bpmh})]\}_n\cdot 6n(H_2O)$ (1) and $[Cd_3(bptc)(3\text{-bpmh})(H_2O)_3]_n\cdot 4n(H_2O)$ (2)

The mixture formed by 0.1 mmol of $Zn(NO_3)_2\cdot 6H_2O$, 0.05 mmol of H_3bptc, 0.05 mmol of 3-bpmh, 8 mL of deionized H_2O, and 1 drops of NaOH solution with a concentration of 0.5 mol/L was sealed to a small glass vial (20 mL) and the obtaining product was heated for three days at 110 °C temperature. After the mixture was naturally cooled to the environmental temperature gradually, the compound's colorless block crystals of **1** were achieved with yield of 38% in the light of H_3bptc. Anal. calcd. (%) for $C_{81}H_{66}N_{12}O_{25}Zn_4$: C, 52.01; H, 3.53; N, 8.99. Found (%): C, 51.96; H, 3.57; N, 9.02. IR (KBr pallet, cm^{-1}): 3354(s), 2836(m), 1600(s), 1551(s), 1506 (m), 1490(m), 1455(s), 1433(m), 1386(m), 1366(m), 1337(s), 1312(s), 1180(w), 1149(m), 1108(s), 1008(w), 947(w), 907(w), 843(m), 769(m), 737(m), 707(m), 687(m), 613(w), 598(w), 562 (w), 491(m).

The mixture formed by 0.1 mmol of $Cd(NO_3)_2\cdot 4H_2O$, 0.05 mmol of H_3bptc, 0.05 mmol of 3-bpmh, 8 mL of deionized H_2O, and 1 drops of NaOH solution with a concentration of 0.5 mol/L was sealed to a small glass vial (20 mL) and the obtaining product was heated for three days at 110 °C temperature. After the mixture was naturally cooled to the environmental temperature gradually, the compound's colorless block crystals of **2** were achieved with yield of 42% in the light of $Cd(NO_3)_2\cdot 4H_2O$. Anal. calcd. (%) for $C_{42}H_{38}Cd_3N_4O_{19}$: C, 40.65; H, 3.04; N, 4.52. Found (%): C, 40.68; H, 3.04; N, 4.55. IR(KBr pallet, cm^{-1}): 3423(s), 3063(m), 2934(m), 2783(m), 1593(s), 1563(s), 1489(s), 1451(s), 1380(m), 1364(m), 1338(s), 1312(s), 1233(s), 11[illegible](m), 1150(m), 1108(s), 1026(m), 1005 (m), 925(s), 836(m), 776(s), 756(s), 710(m), 689(s), 618(w), 580(w), 535(s).

2.3. X-ray crystallography

The data of single crystal of **1**–**2** were harvested through the graphite–monochromated Mo–*K*α radiation (with λ of 0.71073 Å) at room temperature via exploiting Mercury CCD diffractometer controlled via the computer. By utilizing the dual direct means, the compound's architecture can be solved with *ShelxT*, and then the *SHELXL*-2014 is applied for refinement via full-matrix least square technique on the basis of F^2 (Sheldrick, 2015). The lattice water molecules of **1**–**2** were squeezed out by the PLATON program (van der Sluis and Spek, 1990). The related crystallographical data of **1**–**2** are revealed in Table 1. The chose bond angles (°) and lengths (Å) of the compound of **1**–**2** are exhibited in the Table S1.

2.4. IL-6 and SVCAM-1 detection

For the sake of determining the inhibitory effect of compounds **1** and **2** on the releasing of IL-6 and SVCAM-1 into the serum by EC, the ELISA detection was finished in the work. This research was accomplished fully adhere to the instructions with minor change. Shortly, Pregnant SD rats applied in this work were purchased from the Shanghai Southern Model Biotechnology Co., Ltd. The overall operation of this experiment had gained approval from Animal Ethics Committee of China. Then, pituitrin was injected into the animal in order to lead to the angina animal model. Afterwards the complex was treated at the concentration of 5 mg/kg. The IL-6 and SVCAM-1 released into the serum was measured with ELISA.

Table 1 The crystallographical data for **1**–**2**.

Sample	1	2
Formula	$C_{81}H_{66}N_{12}O_{25}Zn_4$	$C_{42}H_{38}Cd_3N_4O_{19}$
Fw	1868.90	1239.93
Crystal system	monoclinic	monoclinic
Space group	*C*2/c	$P2_1/c$
a (Å)	14.032(3)	14.546(12)
b (Å)	21.758(5)	36.34(3)
c (Å)	28.025(10)	13.132(10)
α(°)	90	90
B(°)	104.281(7)	96.491(14)
γ(°)	90	90
Volume (Å^3)	8292(4)	6897(9)
Z	4	4
Density (calculated)	1.395	1.125
Abs. coeff. (mm^{-1})	1.217	0.963
Total reflections	35,516	10,310
Unique reflections	9464	3127
Goodness of fit on F^2	1.104	1.049
Final *R* indices [$I > 2\text{sigma}(I^2)$]	$R = 0.0845$, $wR_2 = 0.2065$	$R = 0.0847$, $wR_2 = 0.1908$
R (all data)	$R = 0.1127$, $wR_2 = 0.2255$	$R = 0.1283$, $wR_2 = 0.2081$
CCDC	2,092,155	2,092,156

2.5. Real time RT-PCR

To determine the inhibitory influence of compounds **1** and **2** on the Notch signaling pathway activation in the EC after compound treatment, the real time RT-PCR was conducted during the process of research. This experiment was performed strictly complying with the protocols accompanied by some modifications. Shortly, the Pregnant SD rats utilized in this work were acquired from the Shanghai Southern Model Biotechnology Co., Ltd. The overall operation of this experiment had gained approval from Animal Ethics Committee of China. Then, the pituitrin was injected into the animal in order to lead to the angina animal model. Afterwards the complex was treated at the concentration of 5 mg/kg. We gathered the EC and entire RNA in the cells were extracted with TRIZOL reagent. The subsequent steps to observe and measure the entire RNA's concentration. Afterwards, it completed the reverse transcript into cDNA. Lastly, the measurement of the relative expression of the notch was made by the method of real time RT-PCR.

2.6. Flow cytometry

The flow cytometry assay was exercised in this work to determine peripheral blood white blood cell (WBC) numbers of different groups after compounds disposal. This application was accomplished fully according to the instructions with minor change. Shortly, the pituitrin was injected into the animal to lead to the angina animal model. Afterwards, we disposed the compound at the concentration of 5 mg/kg. Next, peripheral blood of total animal was harvested and then labeled with CD34/CD11. Subsequently, the flow cytometry was to measure the absorbance of each sample at least three times, and the levels of WBC were measured. This result was presented as mean ± SD.

2.7. OCTxxx

OCT can quantitatively analyze the main components of plaque, and display the lumen information more clearly, which is conducive to more accurate understanding of the patient's condition and selection of appropriate treatment methods. This detection was conducted completely followed instruction of protocols accompanied by limited adjustments. Shortly, pituitrin was injected into the animal to lead to the angina animal model. Afterwards, we disposed the compound at the concentration of 5 mg/kg. After such treatment, OCT preformation was conducted and the thickness of the fibrous cap of atherosclerotic plaque was determined.

3. Results and discussion

3.1. Crystal structure of compound 1

Single crystal X-ray structural analysis revealed that the fundamental unit of **1** consists of two Zn(II) ions, one and a half bptc^{3-} ligands, one and a half 3-bpmh ligands, a half H_3O^+ ion, as well as the lattice water molecules, which crystallized in the monoclinic C2/c space group. As what we can observe from the Fig. 2a, both Zn1 and Zn2 display trigonal bipyramidal geometries. For Zn1, it is five-coordinated by 3 carboxylate oxygen atoms (O1, O2a together with O5b) from three distinct bptc3- ligands, and 2 pyridyl nitrogen atoms (N1 together with N4) from 2 distinct 3-bpmh ligands. With respect to Zn2, the every coordination of its consists of 4 carboxylate oxygen atoms (O3, O7, O9d, O4e) from 4 independent bptc^{3-} ligands along with 1 pyridyl nitrogen atom (N5) from 1 3-bpmh ligands. The Zn-O distances (1.943(4)-2.126(4) Å) and Zn-N distances (2.202(5)-2.229(5) Å) around Zn(II) ions are both in the regular scope, based on the reported Zn(II) compounds (Kan et al., 2012). The bptc^{3-} ligands in **1** are able to be separated into two different types based on mode of coordination: one adopts a $(\eta^1{:}\eta^0)$-$(\eta^1{:}\eta^0)$-$(\eta^1{:}\eta^1)$-μ_4 mode with the dihedral of 13.45° between two benzene rings, the other adopts a $(\eta^1{:}\eta^1)$-$(\eta^1{:}\eta^0)$-$(\eta^1{:}\eta^0)$-μ_5 mode with the dihedral of 20.32° between two benzene rings (Fig. 1a and 1b). Two symmetry-related Zn1 ions are linked by two bis-monodentate carboxylate groups, affording a dinuclear $[Zn_2(COO)_2]$ subunit with the Zn···Zn distance (4.13 Å), and two symmetry-related Zn2 ions are also bridged by three bis-monodentate carboxylate groups, generating another dinuclear $[Zn_2(COO)_3]$ subunit with the Zn···Zn distance (3.57 Å) (Fig. 2b). These different dinuclear subunits are finally bridged by bptc^{3-} together with 3-bpmh ligands, extending into a complicated three-dimensional skeleton (Fig. 2c). Topologically speaking, by viewing bptc^{3-} ligands, dinuclear $[Zn_2(COO)_2]$ subunits together with dinuclear $[Zn_2(COO)_3]$ subunits as 3-, 6-, 7-linked nodes and 3-bpmh ligands as linear linkers (Fig. S1). As far as we know, skeleton of **1** stands for an unheard-of (3,6,7)-linked topological network with the point symbol of $\{4{\cdot}6^2\}_2\{4^2{\cdot}6^{10}{\cdot}7{\cdot}8^2\}\{6^{13}{\cdot}7^4{\cdot}8^4\}\{6^3\}$ (Fig. 2d).

3.2. Crystal structure of compound 2

If we use Cd(II) ions to substitute Zn(II) ions, we can acquire another new compound **2** that crystallizing in the monoclinic

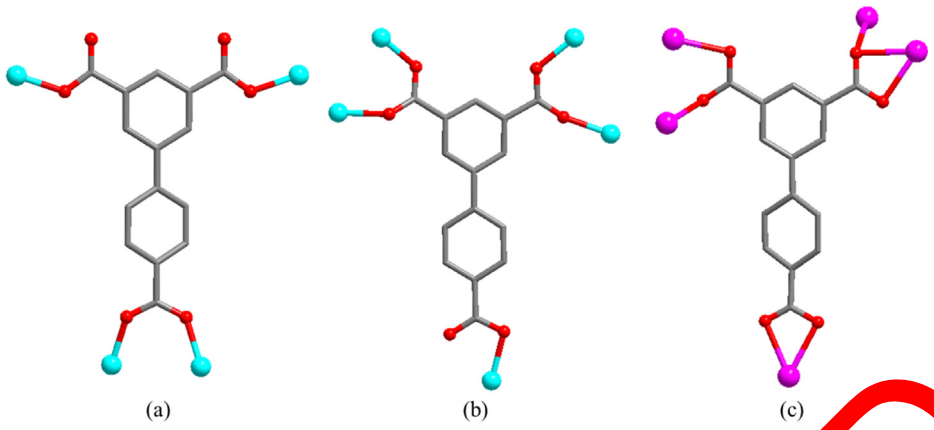

Fig. 1 The coordination modes of bptc3- ligand (a) and (b) for **1**, (c) for **2**

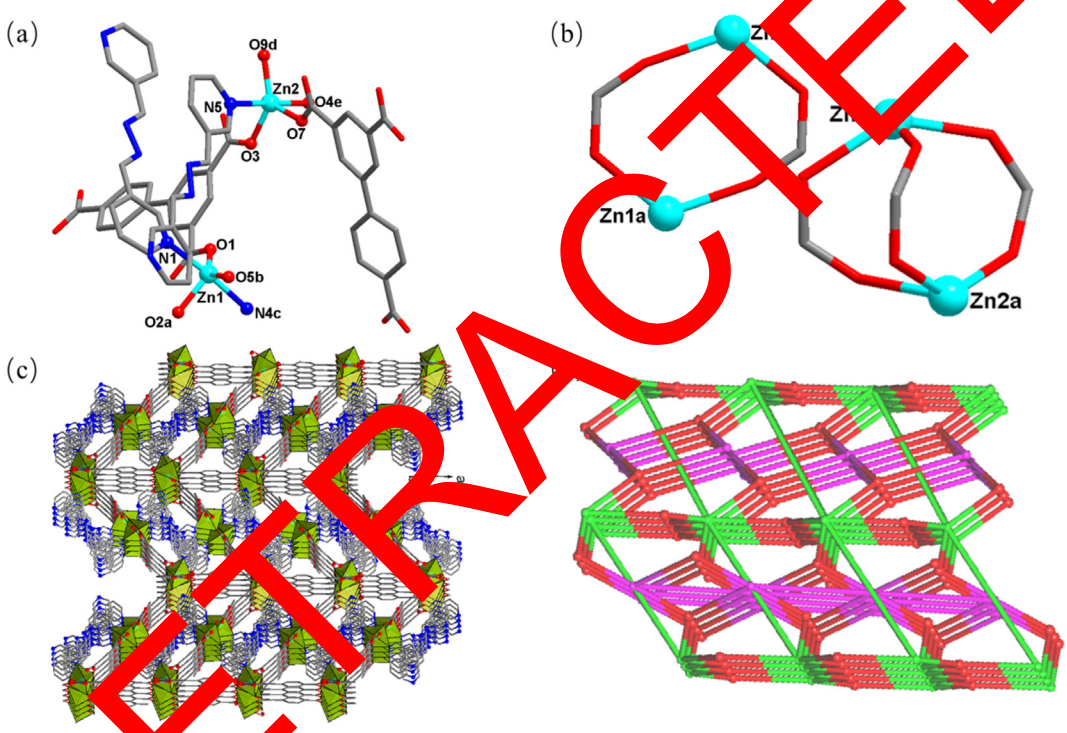

Fig. 2 (a) Viewing of the coordination environment of Zn(II) ion in **1**. (b) Dinuclear $[Zn_2(COO)_2]$ and $[Zn_2(COO)_3]$ subunits in **1**. (c) Complicated three-dimensional skeleton of **1**. (d) Schematic representation of (3,6,7)-linked topological network for **1**.

$P2_1/c$ space group was obtained. Asymmetric unit of **2** covers 3 crystallographically independent Cd(II) ions, 2 $bptc^{3-}$ ligands, 1 3-bpmh ligands, 3 coordinated water molecules together with 4 lattice water molecules. As what we can observe from Fig. 3a, the every six coordination of Cd1 consists of 4 carboxylate oxygen atoms (O5a, O6a, O10b,O11) from 3 distinct $bptc^{3-}$ ligands, along with 2 terminal aqua ligands (O1w and O2w), affording a slightly distorted octahedral geometry. The every seven coordination of Cd2 consists of six carboxylate oxygen atoms (O1, O2, O12, O9b, O10b, O6a) from 4 distinct $bptc^{3-}$ ligands, together with 1 terminal aqua ligand (O3w), showing a slightly distorted pentagonal bipyramidal geometry. Cd3 displays a slightly octahedral geometry. And the coordination of Cd3 consists of 4 carboxylate oxygen atoms (O3, O4c, O7c, O8c) from 3 distinct $bptc^{3-}$ ligands together with 2 pyridyl nitrogen atoms (N1d, N4) from 2 distinct 3-bpmh ligands. Bond distances around Cd(II) ions are in the scope of 2.241(10)-2.512(9) Å. These data are totally in the regular range based on reported Cd(II) MOFs (Dong and Meng, 2018). In **2**, Two crystallographically independent $bptc^{3-}$ ligands show the same coordination mode of $(\eta^1{:}\eta^1)$-$(\mu_2{:}\eta^1)$-$(\mu_1{:}\mu_1)$-μ_5 (Fig. 1c) and features different twist angles of 22.30° and 31.49° between two benzene rings. Cd1 and Cd2 are bridged by two chelating-bridging and one bis-monodentate carboxylate groups to structure a dinuclear $[Cd_2(COO)_3]$ subunit with the Cd···Cd separation of 3.47 Å,

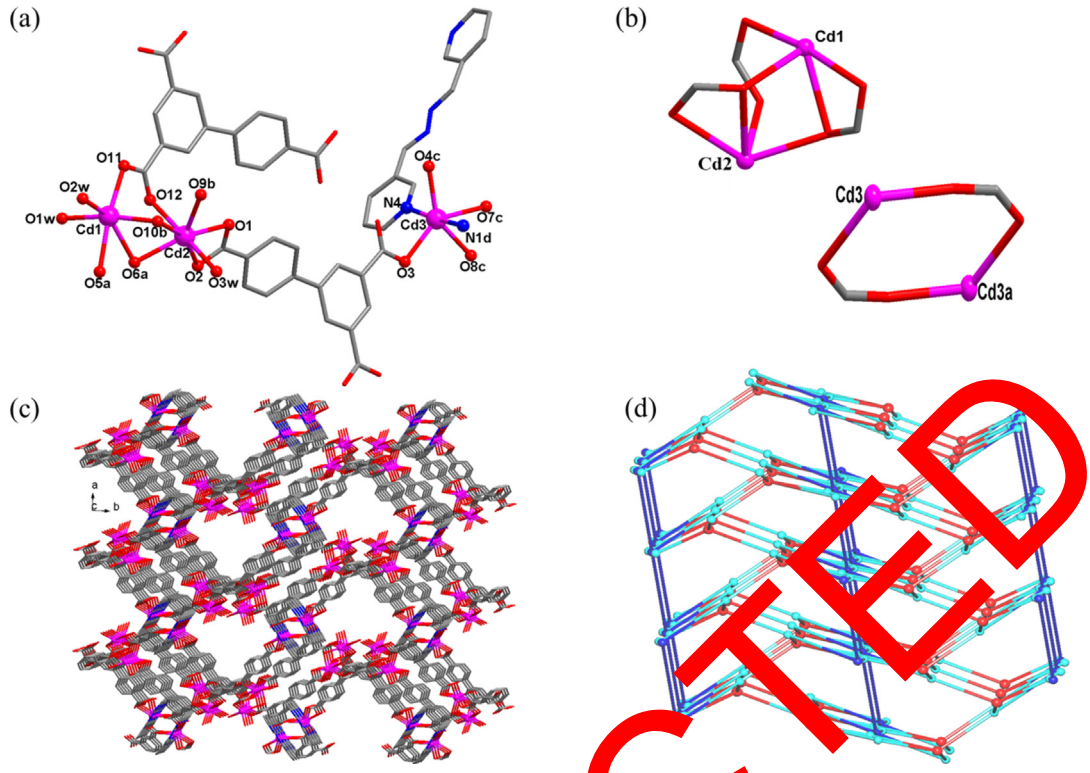

Fig. 3 (a) Viewing of the coordination environments of Cd(II) ions in **2**. (b) Dinuclear $[Cd_2(COO)_2]$ and $[Cd_2(COO)_3]$ subunit. (c) Complicated three-dimensional skeleton of **2**. (d) Schematic representation of the (3,4,6)-linked topological network for **2**.

and two symmetry-linked Cd3 ions are linked by two bridging monodentate carboxylate groups to generate another dinuclear $[Cd_2(COO)_2]$ subunit with the Cd···Cd separation of 4.105 Å (Fig. 3b). Finally, these dinuclear subunits are connected through $bptc^{3-}$ together with 3-bpmh ligands, leading to complicated three-dimensional skeleton (Fig. 3c). For the sake of better understanding of this intricate skeleton, the approach of topological analysis was adopted to simplify it. By viewing $bptc^{3-}$ ligands, $[Cd_2(COO)_3]$ subunits, dinuclear $[Cd_2(COO)_2]$ subunits as 3-, 4-, 6-linked nodes, respectively (Fig. S2), and 3-bpmh ligands as linear connectors, skeleton of **2** is able to be simplified into an unprecedented (3,4,6)-linked topological network with the point symbol of $\{4\cdot7^2\}_2\{4^2\cdot6\cdot7^2\cdot9\}2\{4^2\cdot6\}_2\text{-}\{4^2\cdot7^6\cdot9^2\cdot10^3\cdot11\cdot12\}$ (Fig. 3d).

3.3. Powder X-ray diffraction patterns (PXRD) and thermogravimetric analyses (TGA)

PXRD characterization technology was used to verify the phase purity of a-synthesized bulk samples. It can be seen from

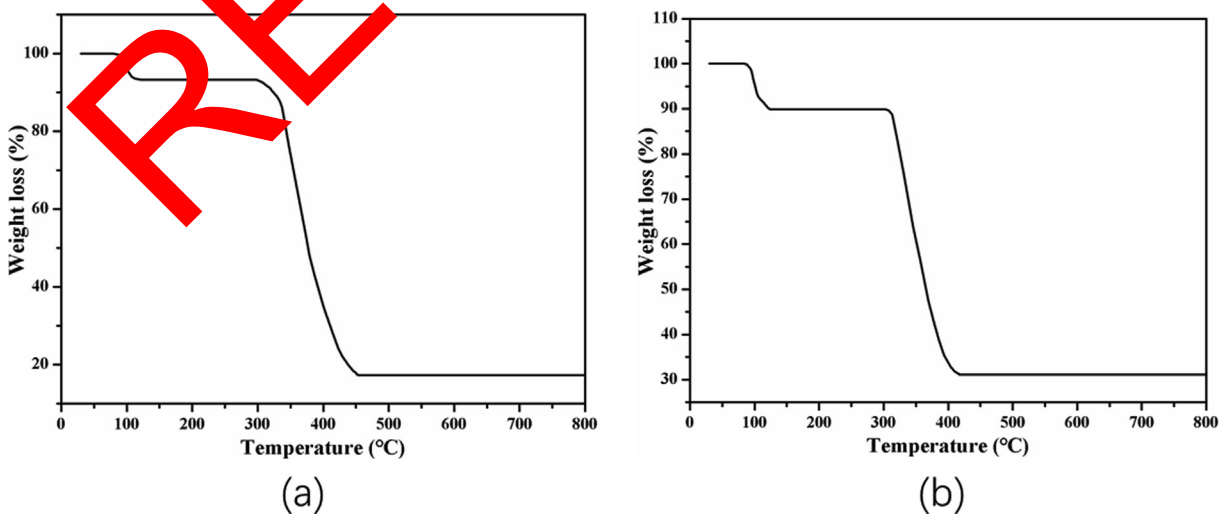

Fig. 4 The TGA curves (a) for **1** and (b) for **2**.

Fig. S3 that a fine agreement exists between experimental patterns and corresponding simulated modes on the account of single crystal diffraction information, indicating good phase purity of obtained samples.

TGA research was employed to discover thermal stabilities of **1**–**2** under nitrogen atmosphere. The TGA results are shown in Fig. 4. From the TGA curves, we can observe that compounds **1**–**2** exhibit a two-step weight loss process. For **1**, weight loss of first step in the scope of 80–114 °C is associated with removal of lattice water molecules (obsd: 6.78%, calcd: 6.74%), and organic ligands' decomposition contributes to the second weight loss, which began at 297 °C and ended at 454 °C, leaving the final residues with a weight of 17.24% that corresponds to the generation of ZnO (calcd: 17.42%). For **2**, the first-step weight loss of 10.09% occurred from 84 to 123 °C and can originate from the loss of the terminal aqua ligands together with lattice water molecules. Weight loss of second step in the scope of 303–418 °C is associated with removal of organic ligands. The final residues with a weight of 31.02% were assigned to the formation of CdO (calcd: 31.07%).

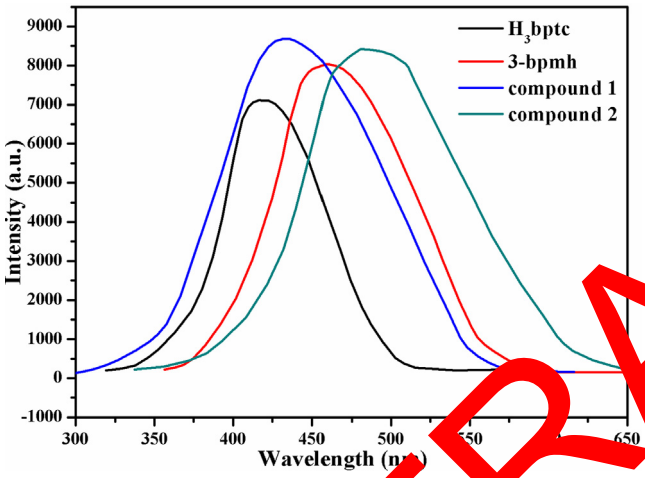

Fig. 5 The luminescent emission spectra of **1**–**2** and corresponding free organic ligands under room temperature.

3.4. Luminescent properties of compounds 1–2

Inspired by brilliant luminescent properties of d^{10} transition metal-based MOFs (Chen et al., 2016; Yu, 2017), herein, we measured luminescent spectra of **1**–**2** and corresponding organic ligands in the environment of room temperature. Free H_3bptc along with 3-bpmh ligands shows broad emission bands with the maximum peaks at 418 nm (λ_{ex} = 322 nm) and 459 nm (λ_{ex} = 340 nm) separately (Fig. 5), that is possible to lead to $\pi^* \rightarrow \pi/n$ transition (Li et al., 2017). And compounds **1**–**2** also show intense luminescence with emission bands centered at 433 nm (λ_{ex} = 350 nm) and 480 nm (λ_{ex} = 350 nm) separately. It is noteworthy that luminescent emission peak of **1** locates between those of H_3bptc and 3-bpmh ligands, and the luminescent emission peak of **2** exhibit obvious red-shift compared to those of H_3bptc and 3-bpmh ligands. According to the reports, it is well known that Zn(II) and Cd(II) ions have difficulties in reduction or oxidization, thus, luminescence of **1**–**2** is possibly to be attributed to intraligand or interligand charge transfer. Different luminescent behaviors of **1**–**2** are possible to result from different structures and coordination patterns of organic ligands.

3.5. Inhibited IL-6 and SVCAM-1content released by the EC under compound treatment

Further than synthesis of compounds **1** and **2** with new structures, biological activity of novel complex was discovered. Thus, IL-6 along with SVCAM-1content released by EC after indicated disposal was measured. The results in Fig. 6 indicated that there was improved degree of IL-6 along with SVCAM-1content in the model group in the contrast of control group. After the treatment of compound **1**, the IL-6 and SVCAM-1content was significantly reduced. While, complex

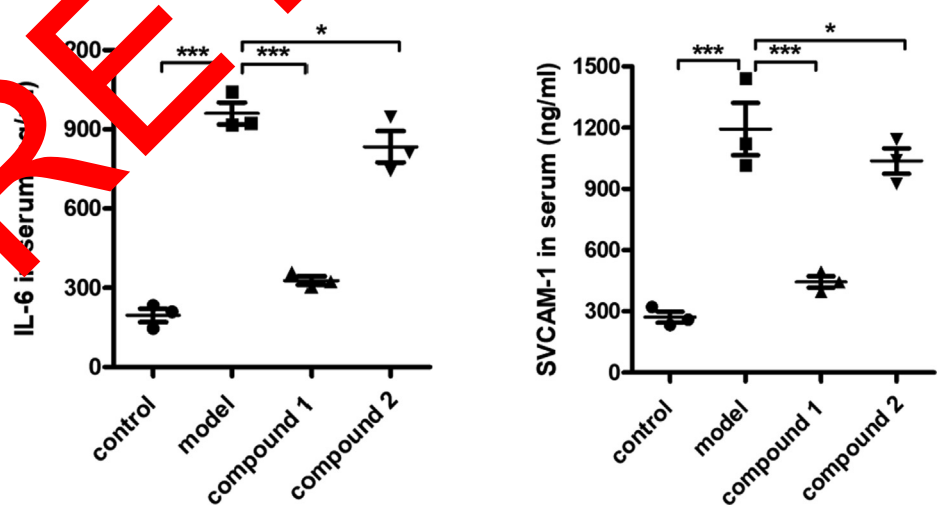

Fig. 6 Compound significantly reduce the IL-6 and SVCAM-1content released by the EC. The angina pectoris animal model was created while compounds were disposed at the concentration of 5 mg/kg. IL-6 and SVCAM-1content released by EC under complex disposal was measured with ELISA.

2 revealed a much weaker influence on IL-6 and SVCAM-1content than compound **1**.

3.6. Reduced activation of the Notch signaling pathway in the EC later than complex disposal

It suggests that the compound significantly reduced IL-6 and SVCAM-1content released by the EC from the above-mentioned studies. As the Notch signaling pathway in the EC regulated the releasing of IL-6 and SVCAM-1, so, the real time RT-PCR was further utilized and activation of Notch signaling pathway in the EC was detected. It is revealed in Fig. 7 that the abnormal increased level of Notch signaling pathway could be reduced by compound **1**, but not compound **2**.

3.7. Inhibitory effect of the compound on the levels of WBC numbers

The changes in the number of white blood cells have the significant importance on the occurrence, development and prognosis of ischemic heart disease. The previous researches showed that the degree of white blood cell elevation is related to the prognosis of patients with acute myocardial infarction. Thus, in this present research, the WBC numbers after compound treatment was determined with flow cytometry. It is revealed from Fig. 8 that the levels of WBC numbers were much higher in the model group than the control group, with $P < 0.005$. After the treatment of compound **1**, the levels of WBC numbers were distinctly decreased, which is more significant than the effect of compound **2**.

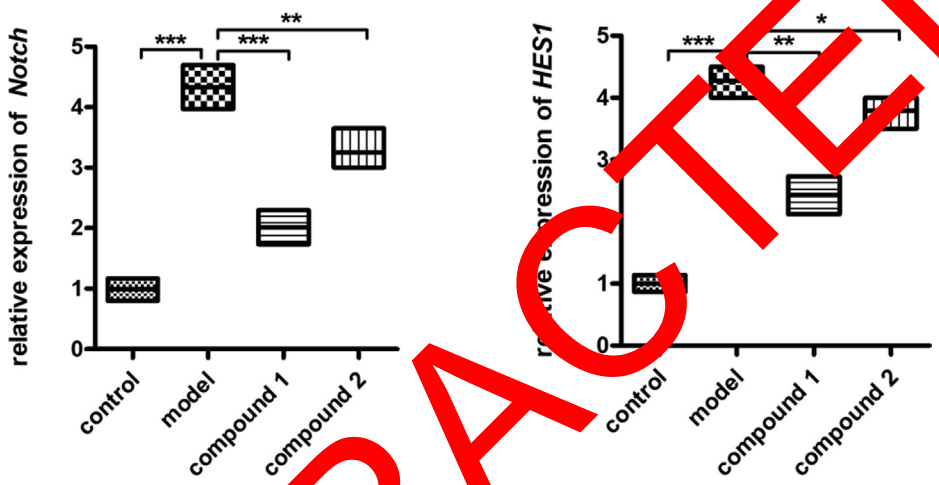

Fig. 7 Compound obviously reduce the Notch signaling pathway activation in EC. Angina pectoris animal model was created while compounds were disposed at the concentration of 5 mg/kg. Real time RT-PCR was used to estimate the Notch signaling pathway activation in EC.

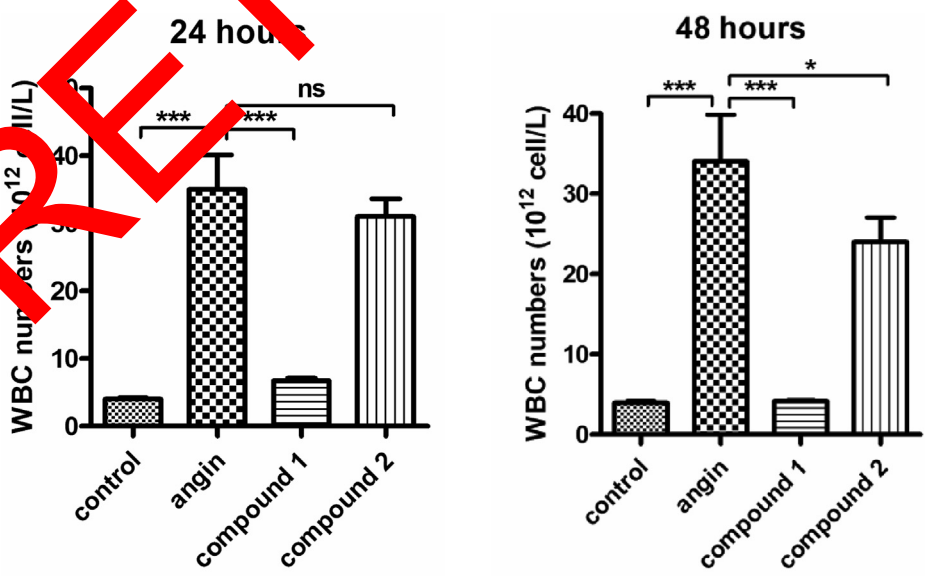

Fig. 8 Compound obviously reduce the levels of WBC numbers. The angina pectoris animal model was created and compounds were disposed at the concentration of 5 mg/kg. flow cytometry was performed and the levels of WBC numbers was determined.

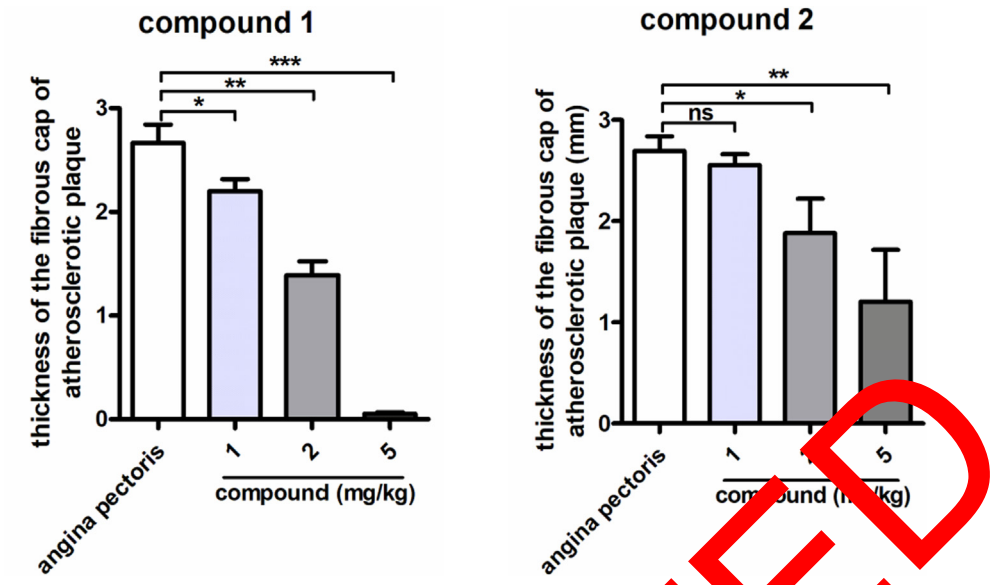

Fig. 9 Obviously reduced thickness of the fibrous cap of atherosclerotic plaque in patients with angina pectoris after compound treatment. The angina pectoris animal model was created and compounds were disposed at the concentration of 5 mg/kg. OCT was used to measure the thickness of the fibrous cap of atherosclerotic plaque in patients with angina pectoris.

3.8. Compound obviously reduce thickness of the fibrous cap of atherosclerotic plaque in patients with angina pectoris

During the procession of angina pectoris, there was a significantly character of fibrous cap of atherosclerotic plaque in patients. So, OCT was used to measure the thickness of the fibrous cap of atherosclerotic plaque in patients with angina pectoris after compound disposal. It is exhibited in Fig. that thickness of the fibrous cap of atherosclerotic plaque in patients with angina pectoris could be significantly reduced by compound **1**. This inhibition of the compound **1** was much stronger than the inhibitory activity of compound **2**, which is consistence with the previous study.

4. Conclusions

Two new coordination polymers on the basis of the mixed bptc^{3-} together with 3-bpmh ligands have been synthesized in success *via* tuning the central metal ions from Zn(II) to Cd(II) under hydrothermal conditions. Both **1** and **2** have an extended framework based on two different dinuclear [$M_2(COO)_2$] and [$M_2(COO)_3$] subunits (M = Zn, Cd), but they represent different network topologies: unprecedented (3,6,7)-connected topology for **1** and unprecedented (3,4,7)-connected topology for **2**. Intense luminescent emissions of **1**–**2** at room temperature demonstrate that they are able to be served as good photoactive materials. The results of the ELISA detection showed that compound **1** had a better performance on reducing the IL-6 and SVCAM-1content released by the EC compared to compound **2**. Besides, the data of the real time RT-PCR showed that compound **1** distinctly reduced activation of Notch signaling pathway in the EC. The WBC numbers in compound **1** treatment group was much lower than that of compound **2** treatment group. Thickness of fibrous cap of atherosclerotic plaque in patients with angina pectoris was strongly decreased by compound **1** instead of compound **2**. At last, we can arrive at this conclusion, compound **1** was much stronger than compound **2** on angin treatment by reducing the IL-6 and SVCAM-1content released by the EC.

5. Data Availability

Selected bond lengths (Å) and angles (°) for compounds **1**–**2** (Table S1); The defined 3-connected, 6-connected, and 7-connected nodes for **1** (Fig. S1); The defined 3-connected, 4-connected, and 6-connected nodes for **2** (Fig. S2); The PXRD patterns (a) for **1** and (b) for **2** (Fig. S3), the information could be found in the supporting information file.

Funding

The research was supported by the National Natural Science Foundation of China (81770426) and Open Subject of the Key Laboratory of Myocardial Lschemia of Ministry of Education (KF202116).

Declaration of Competing Interest

The authors declare that they have no known competing financial interests or personal relationships that could have appeared to influence the work reported in this paper.

Appendix A. Supplementary material

Supplementary data to this article can be found online at https://doi.org/10.1016/j.arabjc.2021.103566.

References

Fuchs, R.M., Becker, L.C., 1982. Pathogenesis of angina pectoris. Arch. Intern. Med. 142, 1685–1692.
Kelemen, M.D., 2006. Angina pectoris: evaluation in the office. Med. Clin. North Am. 90, 391–416.
Zuchi, C., Tritto, I., Ambrosio, G., 2013. Angina pectoris in women: focus on microvascular disease. Int. J. Cardiol. 163, 132–140.

Fan, L., Zhao, D., Zhang, H., Wang, F., Li, B., Yang, L., Deng, Y., Zhang, X., 2021. A hydrolytically stable amino-functionalized Zinc (II) metal-organic framework containing nanocages for selective gas adsorption and luminescent sensing. Micropor. Mesopor. Mat. 326, 111396.

Fan, L., Zhao, D., Li, B., Wang, F., Deng, Y., Peng, Y., Wang, X., Zhang, X., 2022. Luminescent binuclear Zinc(II) organic framework as bifunctional water-stable chemosensor for efficient detection of antibiotics and Cr(VI) anions in water. Spectrochim. Acta Part A Mol. Biomol. Spectrosc. 264, 120232.

Wang, F., Tian, F., Deng, Y., Yang, L., Zhang, H., Zhao, D., Li, B., Zhang, X., Fan, L., 2021. Cluster-Based Multifunctional Copper (II) Organic Framework as a Photocatalyst in the Degradation of Organic Dye and as an Electrocatalyst for Overall Water Splitting. Cryst. Growth Des. 21, 4242–4248.

Zhao, D., Song, J., Zhang, X., Wang, F., Li, B., Yang, L., Deng, Y., Li, Q., Fan, L., 2021. A pillar-layered binuclear 3D cobalt(ii) coordination polymer as an electrocatalyst for overall water splitting and as a chemosensor for Cr(vi) anion detection. CrystEngComm 23, 6245–6252.

Zhang, D., Bi, C., Zong, Z., Fan, Y., 2020. Three different Co(II) metal–organic frameworks based on 4,4'-bis(imidazolyl)diphenyl ether: syntheses, crystal structure and photocatalytic properties. J. Inorg. Organomet. P. 30, 5148–5156.

Li, R.F., Li, R.H., Liu, X.F., Chang, X.H., Feng, X., 2020. Lanthanide complexes based on a conjugated pyridine carboxylate ligand: structures, luminescence and magnetic properties. RSC Adv. 10, 6192–6199.

Li, R.F., Zhang, Y.W., Liu, X.F., Chang, X.H., Feng, X., 2020. The synthesis, structural elucidation and fluorescent sensitization detection to Hg^{2+} based on two lanthanide-organic complexes. Inorg. Chim. Acta 502, 119370.

Luo, F., Ning, Y., Luo, M.B., Huang, G.L., 2010. Chiral or achiral camphorate-based complexes controlled by the conformational rigidity of N-donor co-ligands. CrystEngComm 12, 2769–2774.

Qin, Y.Y., Zhang, J., Li, Z.J., Zhang, L., Cao, X.Y., Yao, Y.G., 2008. Organically templated metal–organic framework with 2-fold interpenetrated $\{3^3.5^9.6^3\}$-lcy net. Chem. Commun. 2008, 2532–2534.

Ma, C., Du, H., Liu, J., Kang, L., Du, X., Xi, X., Ran, H., 2021. High temperature stability of dielectric and energy-storage properties of weakly-coupled relaxor (1–x)$BaTiO_3$-x$(Y_{1/3}Ti_{1/2})$ ceramics. Ceram. Int. 47, 25029–25036.

Ran, H.P., Du, H.L., Ma, C.Y., Zhao, Y.F., Feng, D.N., Xu, H., 2021. Effects of A/B-Site Co-Doping on Microstructure and Dielectric Thermal Stability of $AgNbO_3$ Ceramics. Sci. Adv. Mate. 13, 741–747.

Ma, L., Liu, Y., Su, F., 2019. Self-assembly of Zn/Cd-coordination polymers based on 3,3',4'-biphenyltetracarboxylic acid and N-donor ligands and luminescent sensing of Fe^{3+} ions. J. Solid State Chem. 269, 6[illegible]/1.

Guo, X.L., Xu, J.N., Su, J., Chen, Z.D., Wang, L., Fan, Y., 2019. Three layer structures of coordination polymers based on flexible 5-(4-pyridyl)-methoxylisophthalic acid: rapid synthesis and luminescence sensing. CrystEngComm 21, 1001–1008.

Zhang, X., Huang, Y.Y., Lin, Q.P., Zhang, J., Yao, Y.G., 2013. Using alkaline-earth metal ions to tune structural variations of 1,3,5-benzenetricarboxylate coordination polymers. Dalton Trans. 42, 2294–2301.

Yang, J.X., Qin, Y.Y., Ye, R.P., Zhang, X., Yao, Y.G., 2016. Employing mixed-ligand strategy to construct a series of luminescent Cd(II) compounds with structural diversities. CrystEngComm 18, 8309–8320.

Zhang, Y., Fan, J., Chen, L.Z., Geng, H.M., 2020. Structural diversities of a series of Zn(II)/Cd(II) coordination polymers constructed via dual-ligand strategy of D-(+)-camphoric acid and pyridine-based ligand. J. Mol. Struct. 1218, 128482.

Feng, X., Feng, Y.Q., Guo, N., Sun, Y.L., Zhang, T., Ma, L.F., Wang, L.Y., 2017. Series d−f heteronuclear metal−organic frameworks: color tunability and luminescent probe with switchable properties. Inorg. Chem. 56, 1713–1721.

Feng, X., Li, R.F., Wang, L.Y., Ng, S.W., Qin, G.Z., Ma, L.F., 2015. A series of homonuclear lanthanide coordination polymers based on a fluorescent conjugated ligand: syntheses, luminescence and sensor. CrystEngComm 17, 7878–7887.

Bu, Y., Jiang, F., Zhou, K., Gai, Y., Hong, M., 2014. From 3D interpenetrated polythreading to 3D non-interpenetrated polythreading: SBU modulation in a dual-ligand system. CrystEngComm 16, 12[illegible]–1252.

Yang, E., Ding, Q., Kang, Y., [illegible], F., 2013. Two photoluminescent metal–organic frameworks with highly-connected topological nets. CrystEngComm 15, 10563–10568.

Zhang, J., Chew, E., Chen, S., Pham, J.T.H., Bu, X., 2008. Three-dimensional homochiral transition-Metal camphorate architectures directed by a flexible auxiliary ligand. Inorg. Chem. 47, 3495–3497.

Sheldrick, G.M., 2015. Crystal structure refinement with SHELXL. Acta Crystallogr. Sect. C: Struct. Chem. 71, 3–8.

van der Sluis, P., Spek, A.L., 1990. BYPASS: an effective method for the refinement of crystal structures containing disordered solvent regions. Acta Crystallogr. Sect. A: Crystallogr. 46, 194–201.

Kan, W.Q., Yang, J., Liu, Y.Y., Ma, J.F., 2012. Effect of organic anions on the self-assembly of Zn(II)-containing coordination polymers based on trigonal N-donor ligands. CrystEngComm 14, 6934–6945.

Dong, Y.L., Meng, X.F., 2018. pH induced structural variation of two new Cd(II) compounds: From 2D layer to 3D pillar-layered framework. J. Mol. Struct. 1164, 89–93.

Chen, S.M., Chen, Y.F., Liu, L., Wen, T., Zhang, H.B., Zhang, J., 2016. Two anionic metal-organic frameworks with tunable luminescent properties induced by cations. J. Solid State Chem. 235, 23–27.

Yu, Y., 2017. Hydrogen bonds directed 2D→3D interdigitated Cd(II) compound: Synthesis, crystal structure and dual-emission luminescent properties. J. Mol. Struct. 1137, 109–112.

Li, L., Wang, S., Chen, T., Sun, Z., Luo, J., Hong, M., 2012. Solvent-dependent formation of Cd(II) coordination polymers based on a C_2-symmetric tricarboxylate linker. Cryst. Growth & Des. 12, 4109–4115.